

OVERVIEW OF TRANSPORT, DAMPING, AND WAVE COUPLINGS FROM SEPARATRIX DISSIPATION IN AN AXISYMMETRIC PLASMA

C. F. Driscoll¹, A. A. Kabantsev¹, D. H. E. Dubin¹, Yu. A. Tsidulko²

¹*Univ. of California at San Diego, 9500 Gilman Drive, La Jolla, CA, 92093 USA*

²*Budker Institute of Nuclear Physics, Prospekt Lavrent'eva 11, Novosibirsk 630090, Russia*

*Axial variations in magnetic or electrostatic confinement fields create local trapping separatrixes, and traditional neo-classical theory analyzes the effects from **collision-induced** separatrix crossings. Recent experiments and theory have characterized the distinctive neo-classical effects from **chaotic** separatrix crossings, induced by equilibrium plasma rotation across θ -ruffled separatrixes, or by wave-induced separatrix fluctuations. Experiments on nominally-symmetric pure electron plasmas with controlled separatrixes agree quantitatively with theory in 3 broad areas: 1) radial particle transport is driven by a static z - and θ -asymmetry; 2) both $E \times B$ drift waves and Langmuir waves are damped; and 3) novel dissipative wave-wave couplings are observed. The new chaotic neo-classical effects scale as $\nu^0 B^{-1}$, whereas traditional plateau-regime collisional effects scale as $\nu^{1/2} B^{-1/2}$.*

I. INTRODUCTION

Most plasma confinement devices have local trapping separatrixes, arising from variations in magnetic field strength or from external potentials. Separately trapped populations of particles may then have substantially different drift orbits, giving rise to large dissipative transport steps when separatrix crossings occur. Neo-Classical Transport (NCT) theory analyzes the particle transport and wave effects arising from *collisional* separatrix scatterings in a variety of geometries [1, 2, 3, 4]; and experimental corroboration has been obtained in some regimes of strong collisions [5, 6].

Recent experiments and theory have now characterized a novel *collisionless* form of NCT, where “chaotic” separatrix crossings occur due to plasma rotation across $\cos(m\theta)$ ruffled separatrixes, or due to wave-induced separatrix fluctuations. This mechanism has previously been taken to be ineffective because of presumed symmetries [7].

The experiments are performed on low-collisionality, strongly magnetized pure electron

plasma columns, with controlled trapping separatrixes. The separatrixes are created by applied wall voltages, or by magnetic field strength variations as small as $\delta B_z/B_z \sim 10^{-3}$; and controlled $\cos(m\theta)$ ruffles are added. Dissipative separatrix effects are then observed in 3 broad areas: 1) Radial particle transport is driven by an overall “error field,” such as a tilt of the magnetic field [8]. 2) For wave damping, the error field is the wave potential itself, and strong damping is observed for both low-frequency drift waves [9] and high frequency plasma waves [10]. 3) Additionally, novel dissipative wave-wave couplings are observed, when one wave modifies the separatrix, thereby modifying the separatrix damping of another wave.

Experiments with controlled separatrix ruffles now unambiguously distinguish the chaotic and collisional contributions. We find that chaotic NCT scales with collision rate and magnetic field as $\nu^0 B^{-1}$, whereas collisional NCT scales as $\nu^{1/2} B^{-1/2}$. The high magnetic field minimizes kinetic bounce-rotation resonance effects [11, 12], which typically scale closer to B^{-2} or B^{-3} .

Theory analyses of ruffled separatrix effects have now been developed from two complementary perspectives. A dynamical bounce-mapping approach characterizes the quasi-steady-state density perturbations, including bounce-resonant effects in regimes of ultra-low collisionality. A second simpler approach [13] *assumes* random (chaotic) separatrix crossings, connects smoothly with collisional NCT, and agrees with the dynamical approach outside the bounce-resonant regimes.

II. APPARATUS

The pure electron plasma columns utilized here are confined in a cylindrical Penning-Malmberg trap [8]. Electrons are confined radially by a nominally uniform axial magnetic field $0.4 < B < 20$ kG; and are confined axially by voltages $V_c = -100$ V on end cylinders

of radius $R_w = 3.5\text{cm}$ (Fig. 1). The electron columns

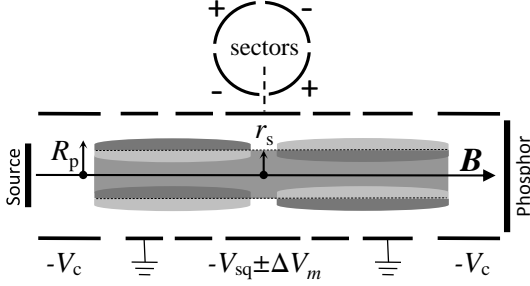


Figure 1: Schematic of the cylindrical apparatus, with ruffled separatrix from V_{sq} and $\pm\Delta V_m$, with TPDM wave on the electron column.

have length $L_p = 49\text{cm}$, and radial density profile $n(r)$ with central density $n_0 = 1.6 \times 10^7\text{cm}^{-3}$ and line density $N_L = \pi R_p^2 n_0 = 6.1 \times 10^7\text{cm}^{-1}$.

The unneutralized charge results in an equilibrium potential energy $\Phi_e(r)$ with $\Phi_{e0} = +28\text{eV}$ at $r = 0$ (here, all Φ 's are in energy units). This gives an $E \times B$ drift rotation $f_E(r)$ which decreases monotonically from $f_{E0} = 230\text{kHz}$ ($B/1\text{kG}$) $^{-1}$. The electrons have a near-Maxwellian velocity distribution with thermal energy $T \lesssim 1\text{eV}$, giving axial bounce frequency $f_b = \bar{v}/2L_p = 430\text{kHz}$ and rigidity $\mathcal{R} \equiv f_b/f_{E0} = 2B_{\text{kG}}$.

An electrostatic trapping barrier ϕ_s is created by a “squeeze” wall voltage V_{sq} with adjustable θ -components. This gives interior separatrix energy $\phi_s(r, \theta) = \phi_{s0}(r) + \Delta\phi_m(r) \cos[m(\theta - \theta_m)]$, as shown schematically in Fig. 2a. Here, we focus on $m = 2$ ruffles, created by voltages $\pm\Delta V_m$ applied to four 60° sectors, extending over $\Delta z = 3.8\text{cm}$ near the $z = 0$ center. At every radius, low energy particles are trapped in either the left or right end, whereas higher energy untrapped particles transit the entire length.

Particles change from trapped to untrapped (and vice versa) due to collisions, due to drift-rotation across θ -ruffles, or due to temporal fluctuations $\Delta\phi_t$ in the separatrix energy. The electron-electron collisionality of the electron plasma is relatively low, spreading parallel velocities at the separatrix by an energy width $\Delta W_c \equiv T(\nu/2\pi f_E)^{1/2}(\phi_{s0}/T)^{1/2} \approx 20\text{meV}$ $B_{\text{kG}}^{1/2}$ during a drift-rotation period. The “chaotic” trapping processes will be important when $\Delta\phi_m \gtrsim \Delta W_c$, or when $\Delta\phi_t \gtrsim \Delta W_c$.

Radial particle transport is driven by global “error fields” varying as $\cos \ell\theta$; here, we focus on static $\ell = 1$, z -anti-symmetric error fields created by a small magnetic tilt (Fig. 1b). The tilt has controlled magnitude $\epsilon_B \equiv B_\perp/B_z \lesssim 10^{-3}$, with chosen tilt angle $\theta_B \equiv \tan^{-1}(B_y/B_x)$, i.e. rotated by $\alpha \equiv \theta_B - \theta_m$ relative to the separatrix ruffle. This tilt is equivalent to applying

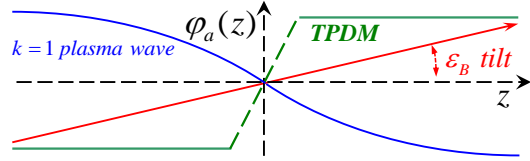
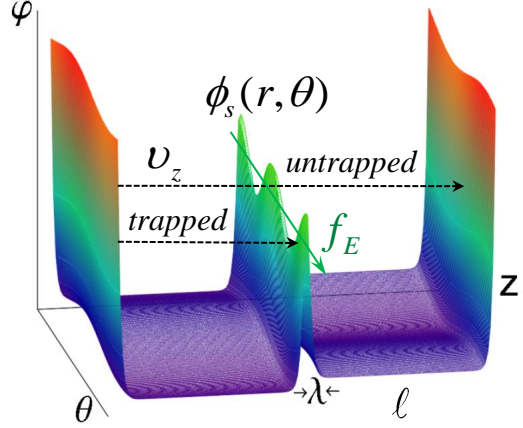


Figure 2: a) θ -symmetric end confinement and central separatrix potentials, modified by an $\ell = 1$ z -antisymmetric error field, and an $m = 2$ ruffle on the separatrix; b) z -dependence of 3 error fields.

wall voltages $V(R_w, \theta, z) = (\epsilon_B z)(2eN_L/R_w) \cos(\theta - \theta_B)$, which causes interior Debye-shielded $\ell = 1$ error potentials $\delta\phi_1(r, z)$.

III. NEO-CLASSICAL THEORY

For large B fields, giving rigidity $R \gg 1$, simple z -bounce-averaged theory suffices to describe the separatrix-induced transport and wave-damping. The tilt-induced error field $\delta\phi_1(r, z)$ has bounce averages $\bar{\delta\phi}_L$ and $\bar{\delta\phi}_R$ for left- and right-end trapped particles near the separatrix energy, with untrapped particles experiencing zero average error field. The drift orbits then differ radially by

$$\Delta r = (\bar{\delta\phi}_L - \bar{\delta\phi}_R)/\overline{\partial\Phi_e/\partial r}. \quad (1)$$

Random transitions between trapped and passing populations are caused by collisions (c); by drift rotation across the $\cos(m, \theta)$ separatrix ruffles (m); and by temporal fluctuations in the separatrix energy (t). If the fraction of particles transitioning in a rotation period is η , the radial diffusion coefficient is expected to be

$$D_r \sim \eta f_E \Delta r^2. \quad (2)$$

For collisions, traditional NCT gives $\eta_c = \Delta W_c F_M(\phi_{s0}) \propto \sqrt{\nu} B^{1/2}$, whereas ruffle η_m and

temporal η_t will be independent of ν and B .

A detailed analysis of random transitions between equal trapping regions driven by rotation across separatrix ruffles gives [13]

$$D_r = \frac{1}{4} \bar{f}_E \Delta r^2 \Delta \phi_M F_M(\phi_{s0}) D_{\ell m}(\alpha), \quad (3)$$

with

$$D_{\ell m} = m \frac{4\ell^2 - m^2 \sin^2 \frac{\pi \ell}{m}}{4\ell^2 - m^2} \begin{cases} 1 & , \frac{2\ell}{m} \notin \text{Int} \\ 2 \sin^2 \ell \alpha & , \frac{2\ell}{m} \in \text{Int} \end{cases}. \quad (4)$$

The dependence on $\alpha \equiv \theta_B - \theta_m$ gives an unambiguous $\sin^2 \alpha$ experimental signature for $\ell = 1, m = 2$.

Equations (3) and (4) can be regarded as the collisionless limit of a more general theory expression for transport that includes collisions. The perturbed particle distribution is written as $\delta f = F_M(K)(-\delta\phi + \omega_r g)/T$ where ω_r is the fluid ($E \times B +$ diamagnetic) rotation frequency, and the nonadiabatic part g solves the bounce-averaged Fokker-Planck equation

$$\bar{\omega}_E \partial g / \partial \theta - Cg = \overline{\partial \delta \phi} / \partial \theta. \quad (5)$$

Here $Cg = 2\phi_{s0} T \nu \partial^2 g / \partial K^2$ is the collision operator, keeping only the highest energy derivative and expanding near $K = V_0$ [1, 2, 7]. The solution of this driven diffusion equation in the trapped and passing regions yields a radial diffusion coefficient given by Eq. (3), except that $D_{\ell m}(\alpha)$ is replaced by $D_{\ell m}(\Delta W_c / \Delta V, \alpha)$.

For $2\ell/m$ integral, Eq. (3) can then be generalized to [13]

$$D_r = \frac{1}{4} \bar{f}_E \Delta r^2 F_M(\phi_{s0}) \{ \Delta W_c D_{cA} + \Delta \phi_M D_{mA} \sin^2 \alpha \}. \quad (6)$$

The collisional bounce-Averaged coefficient D_{cA} is suppressed when ruffles dominate, as $D_{cA} \approx \pi [1 - \exp(-(y/.71)^{5/6})]$, $y \equiv \Delta W_c / \Delta \phi_m$. In contrast, the ruffle contribution is relatively independent of collisions, as $D_{mA} \approx 4[1 - .215 \tanh(y/.6)]$.

Figure 3 shows the enhanced diffusion predicted by Eq. (6) when $\Delta \phi_m > \Delta W_c$, with simple particle simulations (at one radius) corroborating the theory. The full radial flux then has both mobility and diffusive contributions, as

$$\Gamma_r = \mu(\partial \Phi_e / \partial r) - D_r(\partial N_0 / \partial r), \quad (7)$$

with $\mu = D_r N_0 / T$ and $N_0 \equiv \int dz n$.

IV. RADIAL PARTICLE TRANSPORT

Experimentally we diagnose the bulk expansion rate

$$\nu_{\langle r^2 \rangle} \equiv \frac{d}{dt} \langle r^2 \rangle / \langle r^2 \rangle \equiv \int r dr r^2 \frac{1}{r} \frac{\partial}{\partial r} r \Gamma_r / \langle r^2 \rangle. \quad (8)$$

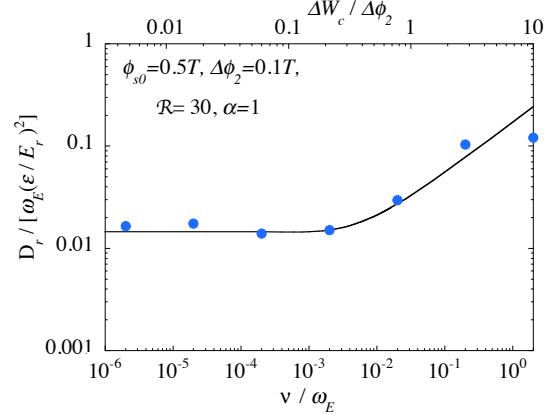


Figure 3: (Color online) Predicted diffusion (curve) and particle simulation results (dots) for weak error field ϵ and ruffle $\Delta \phi_2$, showing enhancement for weak collisionality ν .

Fortunately, $\nu_{\langle r^2 \rangle}$ can be accurately and readily obtained from the frequency $f_{20}(t)$ of a small-amplitude $\ell = 2, k = 0$ diocotron mode, as $\nu_{\langle r^2 \rangle} = -\frac{d}{dt} f_{20} / f_{20}$. This follows from $f_{20} \propto \langle n \rangle = N_L / \langle r^2 \rangle$ with N_L constant; and it has been verified to $\pm 2\%$ by camera images of plasma evolutions.

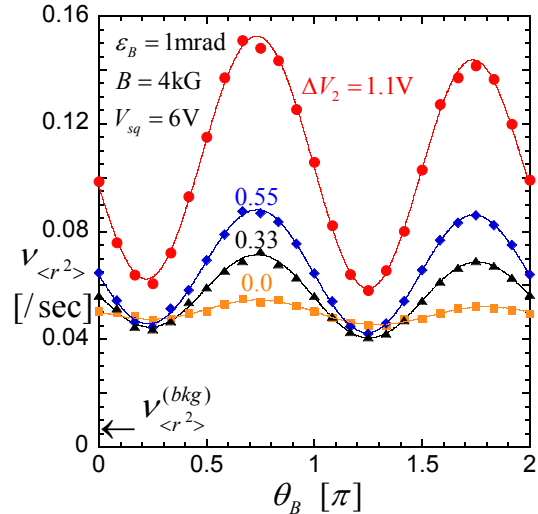


Figure 4: Measured expansion rate $\nu_{\langle r^2 \rangle}$, showing chaotic NCT varying as $\sin^2 \alpha$, and α -independent collisional transport.

Figure 3 is a plot of measured expansion rate $\nu_{\langle r^2 \rangle}$ versus magnetic tilt angle θ_B , for various applied wall ruffle strengths ΔV_m . The ruffled-induced NCT shows an unambiguous $\sin^2 \alpha$ dependence on θ_B , with magnitude proportional to ΔV_m ; and varying θ_m in steps of $\pi/2$ (not shown) verifies the dependence on relative

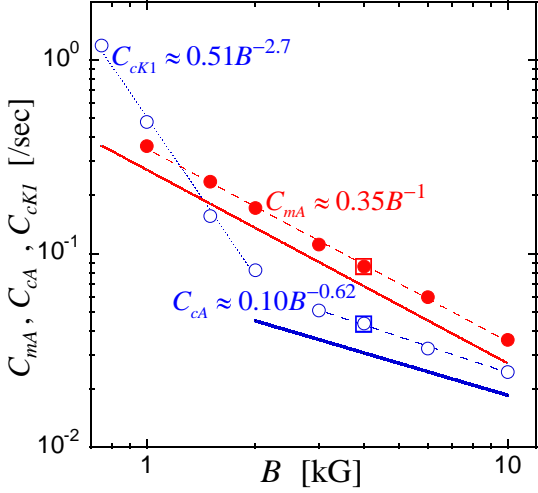


Figure 5: (Color online) Measured transport rates C versus B , with empirical scalings. Solid lines are theory predictions.

angle only.

The distinctive $\sin^2 \alpha$ signature, together with control of ΔV_m and ϵ_B , enables identification of transport processes as

$$\nu_{\langle r^2 \rangle}^{(\text{expt})} = C_{cA} \hat{\epsilon}_B^2 + C_{mA} \hat{\epsilon}_B^2 \Delta \hat{V}_m \sin^2 \alpha + C_{cK1} \hat{\epsilon}_B^2 + C_{cK2} \Delta \hat{V}_m^2 + \nu_{\langle r^2 \rangle}^{(\text{bkg})}. \quad (9)$$

Here, C_{cA} and C_{mA} represent the radial integrals of Eqn. (6) and (7); C_{cK1} and C_{cK2} represent collisional Kinetic (bounce-resonant) transport driven by ϵ_B^2 or ΔV_m^2 as z -dependent “error” fields; and $\nu_{\langle r^2 \rangle}^{(\text{bkg})}$ arises from uncontrolled background tilts, separatrices, and ruffles. For dimensional simplicity, $\hat{\epsilon}_B = \epsilon_B / (1 \text{ mRad})$ and $\Delta \hat{V}_m \equiv \Delta V_m / (1 \text{ Volt})$.

C_{mA} is readily obtained from the $\sin^2 \alpha$ dependence as in Fig. 2, and varying ϵ_B gives the expected $\hat{\epsilon}_B^2$ dependence. Data taken with $\epsilon_B = 0$ shows a $\nu_{\langle r^2 \rangle}^{(\text{bkg})}$ offset and a parabolic dependence on applied ΔV_m , giving C_{cK2} . Varying ϵ_B then selects C_{cA} and C_{cK1} ; these are distinguished by their B -scaling (discussed next), and by the fact that the z -anti-symmetric bounce-averages in C_{cA} require the separatrix, whereas the kinetic C_{cK1} depends only weakly on the applied squeeze voltage.

Figure 4 shows the measured transport rates C_{mA} , C_{cA} and C_{cK1} versus magnetic field with empirical scalings (dashed) compared to theory (lines). At high B , the chaotic and collisional separatrix transport processes agree closely with theory, scaling as B^{-1} and $B^{-1/2}$ respectively. Here the comparison is limited by temperature uncertainty, sensitivity to edge density gradients, and induced modification of $F_M(\phi_{\text{sq}})$.

At low B , the kinetic transport labeled C_{cK1} is observed to depend strongly on field ($\sim B^{-2.7}$), but no simple power-law is expected as bounce-rotation resonances become dominant. Prior scaling experiments have been confused by the presence of uncontrolled separatrices and ruffles, and by overlapping transport regimes [8].

Similar enhanced particle transport is observed when there are *temporal* variations in the separatrix energy. Figure 5 illustrates the immediate increase in radial expansion rate induced when white noise ($V_{\text{RMS}} = 200 \text{ mV}$, $f_{E0} < f < 20 \text{ MHz}$) is applied to the θ -symmetric squeeze ring, driving enhanced random trapped-passing transitions. The $3\times$ increase in $(d/dt)\langle r^2 \rangle$ observed here is consistent with a collisional separatrix layer $\Delta W_c \sim 70 \text{ meV}$ fluctuating by $\Delta \phi_t \sim 200 \text{ meV}$. Presumably, any noise- or wave-induced fluctuations which change particle kinetic energies relative to the separatrix energy would be equally effective in enhancing transport.

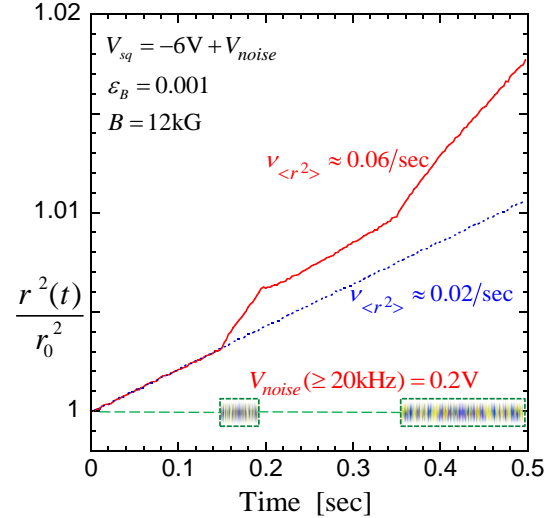


Figure 6: Enhanced expansion rate during two bursts of 200 mV (RMS) noise applied to a 6. V electrostatic separatrix.

Magnetic field ripples are observed to cause similar particle transport [8] with significant transport observed down to our minimum of $\delta B/B \sim 10^{-3}$. Figure 7 shows the vendor-calculated ripples in the CamV superconducting magnet. The original electrode placement had a background loss rate of $\nu_{\langle r^2 \rangle}^{(\text{bkg})} \sim .001$ at $B = 10 \text{ kG}$ due to the separatrix at P . Adding an additional coil to *increase* the mirror strength did not appreciably increase the transport. However, temporarily moving the electrodes to *eliminate* the separatrix reduced this loss rate by $5\times$. Magnetic separatrix effects appear similar to electric separatrix effects, albeit with

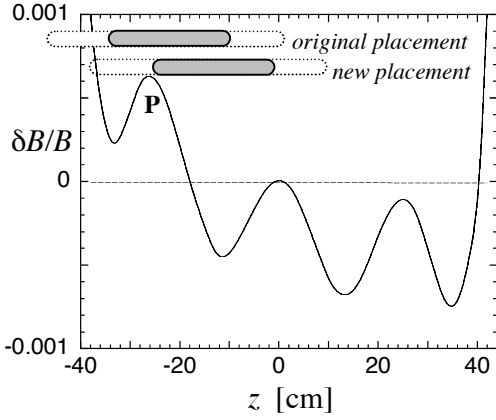


Figure 7: Enhanced expansion rate during two bursts of 200 mV (RMS) noise applied to a 6. V electrostatic separatrix.

different radial dependencies; but magnetic effects are substantially more difficult to study experimentally.

V. WAVE DAMPING

Wave damping due to chaotic and collisional separatrix dissipation is observed for both negative-energy $E \times B$ drift waves and for positive-energy plasma waves. Here, the wave-potential is the “error field” driving transport (Fig. 2b), and the wave frequency enters the generalization of Eq. (6).

Most thoroughly studied is the “Trapped Particle Diocotron Mode” [3, 8] where trapped particles at large radii experience z -anti-symmetric $E \times B$ drifts, while untrapped interior particles provide partial Debye shielding (Fig. 1).

Prior TPDM damping analysis [3] solved for the thin *collisional* boundary layer at the separatrix, as is standard in NCT [1, 2]. This gave quantitative agreement with the experimental observations of TPDM damping rate $\gamma_{1a} \propto B^{-1/2}$ for large B ; but the enhanced damping observed at lower B , scaling as $\gamma_{1a} \propto B^{-1}$, was not understood.

Experiments and theory now establish that the observed B^{-1} scaling of TPDM damping was due to weak, naturally-occurring θ -ruffles on the separatrix. Figure 8a shows the measured γ_{1a} versus strength ΔV_m of an applied static $m = 2$ separatrix ruffle, for two magnetic fields. For $\Delta V_m = 0$, the damping is mostly due to collisions; for larger ΔV_m , the damping increases linearly with ΔV_m as expected for chaotic NCT. Here, $\gamma_{1a} * B$ is plotted, so the identical slopes at $B = 0.4$ and $B = 3$ represent the B^{-1} scaling characteristic of chaotic separatrix processes, analogous to the ΔV_m terms of

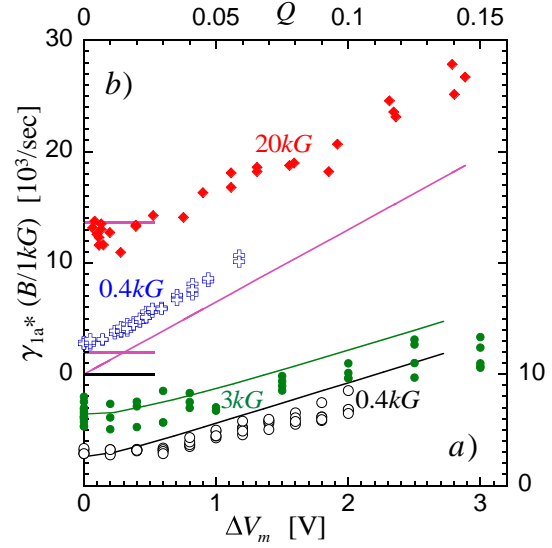


Figure 8: a) (bottom, right scales) TPDM damping rate γ_{1a} times B versus applied ΔV_m for $B = 0.4$ and 3.0 kG. b) (top, left scales) TPDM damping $\gamma_{1a} B$ versus amplitude Q of an excited diocotron mode.

Eq. (9). In contrast, the collisional $\Delta V_m = 0$ intercepts scale as $B^{-1/2}$, and therefore differ by $(3/0.4)^{1/2} = 2.7$. The solid curves of Fig. 8a are the absolute predictions of the probabilistic theory approach, including non-local effects on $n(r, z)$ equilibria [14].

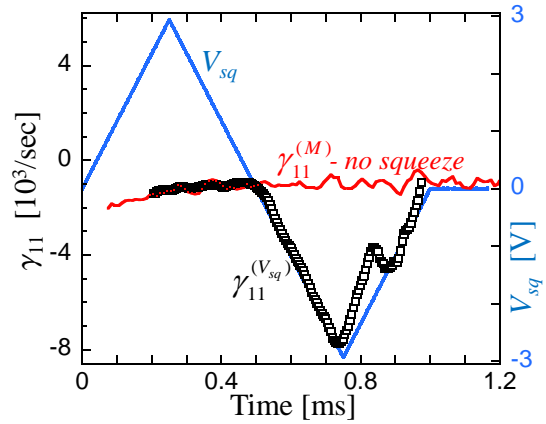


Figure 9: Separatrix damping of a Langmuir wave: $\gamma_{11}^{(M)}$ from a weak magnetic mirror, and $\gamma_{11}^{(V_{sq})}$ due to a triangle-damped negative V_{sq} .

High frequency plasma (Langmuir) waves are also strongly damped by separatrix dissipation, independent of Landau damping effects. Figure 9 shows the measured damping rate γ_{11} for an $\ell = 1$, $k = 1\pi/L_p$ plasma wave with $f_{11} = 1.2$ MHz. This is a large amplitude wave in a “BGK state” of strong wave-particle

trapping. With no applied electrostatic squeeze, damping at rate $\gamma_{11}^{(M)} \sim -1 \times 10^3/\text{sec}$ is observed, due to a naturally occurring *magnetic* separatrix $\delta B_z/B_z \sim 10^{-3}$ peaking near $z = 0$. This magnetic separatrix often dominates background transport also, and removing the separatrix reduces $\nu_{(r^2)}^{(\text{bkg})}$ by up to $5 \times$.

In Fig. 9, adding a triangle-ramped positive (anti-) squeeze wall voltage has no effect on γ_{11} ; but a negative squeeze ramped to -3.Volts immediately and proportionately increases γ_{11} , to a maximum of $\gamma_{11}^{(3V)} = -8 \times 10^3/\text{sec}$. Here, Zakharov-Karpman [15] collisional damping predicts negligible damping, at a rate $\gamma_{11}^{\text{ZK}} \sim -20./\text{sec}$. We also note that excitation of a separate $\ell = 0$ plasma wave to even moderate amplitude immediately increases γ_{11} several fold, due to $\Delta\phi_t$ in the effective energy of the separatrix.

VI. WAVE-WAVE COUPLINGS

The potential associated with one wave can modify the effective separatrix energy seen by particles carrying currents associated with a second wave, thereby damping the second wave. When the waves are resonant and phase-locked, the interaction can be particularly strong.

Figure 8b shows TPDM damping in the presence of a separate $m = 2, k_z = 0$ diocotron mode with frequency $f_{20} \approx f_{E0}$ and controlled quadrupole amplitude Q , with $Q = \Delta/R_0$ for uniform density out to radius $R = R_0 + \Delta \cos 2\theta$ [9]. The diocotron mode creates an $m = 2$ potential $\phi_2(r, z, t)$ at all z , which is *smallest* at the $z = 0$ separatrix, inducing chaotic separatrix crossings proportional to Q . The solid line segments show a $Q = 0$ intercept predicted by collisional NCT [3], and a ruffle-induced enhancement predicted by the bounce-mapping theory, in good agreement with the measurements.

The *resonant* version of this same wave-wave interaction was partially explored in experiments [9] where a large-amplitude $m = 2$ diocotron mode “pump” parametrically decays into an exponentially growing $\ell = 1$ TPDM mode, when parameters are tuned so as to obtain $f_{1a} = f_{20}/2$. The separatrix causes a well-understood conservative mode coupling, exponential instability, and late-time energy sloshing; and the previously puzzling dissipation is now quantitatively understood as TPDM damping from a *phase-locked* $m = 2$ ruffle caused by the pump diocotron mode.

ACKNOWLEDGMENTS

This work was supported by National Science Foundation Grant PHY-0903877 and Department of Energy Grant DE-SC0002451.

References

- [1] P.HELANDER and D.J.SIGMAR, *Collisional Transport in Magnetized Plasmas*, Cambridge Univ. Press (2002).
- [2] M.N.ROSENBLUTH, D.W.ROSS and D.P.KOSTAMOROV, *Nucl. Fusion* **12**, 3 (1972).
- [3] T.J.HILSABECK and T.M.O’NEIL, “Trapped-Particle Diocotron Modes,” *Phys. Plasmas* **10**, 3492 (2003).
- [4] D.H.E.DUBIN, “Theory and Simulations of Electrostatic Field Error Transport,” *Phys. Plasmas* **15**, 072112 (2008).
- [5] T.OHKAWA, *et al.*, *Phys. Rev. Lett.* **28**, 1107 (1972).
- [6] M.C.ZARNSTORFF, *et al.*, “Parallel Electric Resistivity in the TFTR Tokamak,” *Phys. Fluids B* **2**, 1852 (1990).
- [7] H.E.MYNICK, “Transport Optimization in Stellarators,” *Phys. Fluids* **26**, 2609 (1983).
- [8] A.A.KABANTSEV and C.F. DRISCOLL, “Trapped-Particle Modes and Asymmetry-Induced Transport,” *Phys. Rev. Lett.* **89**, 245001 (2002).
- [9] A.A.KABANTSEV, T.M.O’NEIL, Yu.A.TSIDULKO and C.F.DRISCOLL, “Resonant Drift-Wave Coupling Modified by Nonlinear Separatrix Dissipation,” *Phys. Rev. Lett.* **101**, 065002 (2008).
- [10] A.A.KABANTSEV and C.F. DRISCOLL, “Trapped-Particle-Mediated Collisional Damping of Non-Axisymmetric Plasma Waves,” *Phys. Rev. Lett.* **97**, 095001 (2006).
- [11] D.L.EGGLESTON and J.M.WILLIAMS, “Magnetic Field Dependence of Asymmetry-induced Transport: A New Approach,” *Phys. Plas.* **15**, 032305 (2008).
- [12] E.P.GILSON and J.FAJANS, “Quadrupole-Induced Resonant-Particle Transport,” *Phys. Rev. Lett.* **90**, 015001 (2003).
- [13] D.H.E.DUBIN and Yu.A.TSIDULKO, “Neoclassical Transport Caused by Collisionless Scattering across an Asymmetric Separatrix,” *Phys. Rev. Lett.*, submitted (2010).
- [14] T.AKHMETOV and I.KOTELNIKOV, “Equilibrium of Non-neutral Plasmas with Quadrupole Field Errors,” *Phys. Plas.* **16**, 122103 (2009).
- [15] V.E.ZAKHAROV and V.I. KARPMAN, *Sov. Phys. J.E.T.P.* **16**, 351 (1963).